Ultralow-loss tightly confining Si 3 N 4 waveguides and high-Q microresonators

Houssein El Dirani, Laurène Youssef, Camille Petit-Etienne, Sebastien Kerdiles, Philippe Grosse, Christelle Monat, Erwine Pargon, Corrado Sciancalepore

Research Article | Vol. 27, No. 21 / 14 October 2019 / Optics Express 30726
Optics EXPRESS

Ultralow-loss tightly confining Si_3N_4 waveguides and high-*Q* microresonators

HOUSSEIN EL DIRANI,[1] LAURENE YOUSSEF,[2] CAMILLE PETIT-ETIENNE,[2] SEBASTIEN KERDILES,[1] PHILIPPE GROSSE,[1] CHRISTELLE MONAT,[3] ERWINE PARGON,[2] AND CORRADO SCIANCALEPORE[1,*]

[1] *Univ. Grenoble Alpes, CEA-LETI, 38054 Grenoble cedex, France*
[2] *Univ. Grenoble Alpes, CNRS, LTM, 38000 Grenoble, France*
[3] *Institut des nanotechnologies de Lyon, UMR CNRS 5270, Ecole Centrale Lyon, F-69130 Ecully, France*
[*] *corrado.sciancalepore@cea.fr*

Abstract: Efficient nonlinear phenomena in integrated waveguides imply the realization in a nonlinear material of tightly confining waveguides sustaining guided modes with a small effective area with ultra-low propagation losses as well as high-power damage thresholds. However, when the waveguide cross-sectional dimensions keep shrinking, propagation losses and the probability of failure events tend to increase dramatically. In this work, we report both the fabrication and testing of high-confinement, ultralow-loss silicon nitride waveguides and resonators showing average attenuation coefficients as low as ~3 dB/m across the S-, C-, and L bands for 1.6-μm-width × 800-nm-height dimensions, with intrinsic quality factors approaching $\sim 10^7$ in the C band. The present technology results in very high cross-wafer device performance uniformities, low thermal susceptibility, and high power damage thresholds. In particular, we developed here an optimized fully subtractive process introducing a novel chemical-physical multistep annealing and encapsulation fabrication method, resulting in high quality Si_3N_4-based photonic integrated circuits for energy-efficient nonlinear photonics and quantum optics.

1. Introduction

Low propagation losses are crucial for on-chip optical waveguides in several applications such as nonlinear and quantum photonics [1,2], optical gyroscopes [3], and narrow linewidth lasers [4]. Over the last ten years, Si_3N_4-based nonlinear integrated optics has benefited from tremendous advances in fabrication technology and physical understanding [5] of the optical phenomena involved. The resulting coherent optical frequency combs have enabled ultrahigh data rate optical communications [6], low-noise microwave generation [7], and all-optical integrated frequency synthesizers [8].

Energy-efficient nonlinear processes, such as four-wave mixing and frequency conversion, require light-matter interaction to be maximized at the wavelength scale. In addition, coherent optical frequency comb sources require accurately controlled dispersion-engineered waveguides made in low defect bulk materials for time-stable dissipative Kerr soliton (DKS) formation. In order to do so, optical waveguides exhibiting extremely low propagation losses, high power damage thresholds, and the highest possible confinement factor are then necessary.

The highest quality factors ever reported are achieved in silica wedges [9] and MgF_2 whispering gallery modes resonators [10]. In contrast, the nonlinear index of silicon dioxide is low [11] (2.7×10^{-20} m^2/W at 1.5 μm telecom wavelength). In addition, the low refractive index of the silica imposes an air cladding and complicates the integration. That is why high quality factor resonators featuring high refractive index and optical mode high-confinement bring considerable benefits. Moreover, when the refractive index is high (*e.g.*, in silicon), the nonlinear index n_2

#373575 https://doi.org/10.1364/OE.27.030726
Journal © 2019 Received 24 Jul 2019; revised 13 Sep 2019; accepted 22 Sep 2019; published 9 Oct 2019

Optics EXPRESS

tends to be higher. However, the bandgap of the material also tends to be smaller and nonlinear loss processes - such as two-photon absorption (TPA) - generally take place, which is deleterious for energy-efficient nonlinear optics. In this respect, silicon nitride (Si_3N_4) is a trade-off CMOS material that provides, at the same time, relatively high nonlinearity (×10 that of silica), low propagation losses, the absence of direct TPA-related absorption processes, while keeping the ability to obtain high-confinement waveguides.

Recent works based on large, highly multimode waveguides (with cross-sectional widths ranging from 2.5 μm up to 10 μm) have shown ultrahigh quality factors (37×10^6 and 67×10^6) [12–14]. However, such large waveguides limit the ability to obtain high anomalous dispersion, which is a condition for low-power soliton-based comb generation. Moreover, the interaction between different mode families supported by the cavity can prevent the soliton formation as discussed in [15,16], while systematic excess losses due to the inter-mode interactions at the resonator coupling section can occur [17,18]. Tightly confining 1.5–2-μm-wide and 0.75–0.85-μm-thick anomalous dispersion waveguides are then necessary for low-threshold broadband Kerr frequency comb generation at telecoms wavelengths [13], while single-mode low-loss circuitry is needed for efficient quantum optics applications. Another advantage of using tightly confining waveguides is the related increase of the nonlinear parameter γ_{nl}, which is inversely proportional to the waveguide effective mode area A_{eff}.

Tightly confining Si_3N_4 waveguides exhibiting rather attenuation coefficients ranging between 5 dB/m and 6 dB/m have been reported by using the proprietary Damascene reflow process for 1.5-μm-wide waveguides [16,18]. Yet, such approach brings in intrinsically severe film thickness non-uniformity over the wafer, because it involves a chemical mechanical polishing (CMP) step used for the silicon nitride removal after filling the preformed reflowed etched silica. In fact, in such Damascene approach, CMP involves several hundred of nanometers in thickness reduction thus inducing a much higher variance than the typical uniformity of the low-pressure chemical vaporization deposition (< 1% sigma variance), regardless the fabrication tool maturity and wafer scaling. Most importantly, the preform reflow technique used to smoothen out silica pre-trenching sidewalls introduces systematically a strong vertical non-uniformity in the waveguide width (*i.e.*, the sidewalls slope) of several tens or even hundreds of nanometers [18]. The combination of both vertical and horizontal non-uniformities strongly affects the dispersion engineering and the coupling rate from the bus waveguide to the microring, making it more difficult to achieve a deterministic control of the microresonator loading as well as near to critical coupling conditions across a reticule. Whereas, in the case of our fabrication technique, the performed shallow CMP barely affects 5–10 nm of the whole film thickness at most, thus limiting the layer thickness uniformity variance across the wafer.

In this work, we report the fabrication and linear characterization of ultralow-loss tightly confining Si_3N_4 waveguides with attenuation coefficients approaching ~3 dB/m that are key building blocks for nonlinear quantum photonics. These devices are fabricated following a fully subtractive process based on chemical-physical multistep annealing, encapsulation, and a tailored fluorocarbon dry etching of the Si_3N_4 film. Through such processing, which is accessible on a standard fabrication line and widely scalable on large format foundry tools, we *readily* achieve intrinsic quality factors approaching 10^7 for a 200-GHz ring resonator formed by high-confinement anomalous-dispersion waveguides of 1.6-μm-width × 800-nm-height dimensions. Moreover, this approach enables high wafer-scale reproducibility and high power damage thresholds thanks to the low-contamination levels of the as-deposited Si_3N_4 films and the void-free silica encapsulation method. The work will also set guidelines for future breakthroughs, by notably analyzing scattering-related losses as well as bulk- and surface-states-related absorption mechanisms induced by the residual metallic contamination.

This research article is organized as follows. Section II describes the fabrication process, notably the elements of novelty such as the multistep chemical-physical annealing, the fluorocarbon

Optics EXPRESS

plasma etching and proper multilayer encapsulation of the Si_3N_4 waveguides. In Section III, we report the extensive linear optical characterization of such platform by measuring the spectral characteristics of ultra-high Q Si_3N_4 microring resonators. The measurements, performed on a series of nominally identical microrings, provide valuable information on cross-wafer statistics, notably total and intrinsic resonator losses as well as deviations in the critical coupling condition over a 200-mm wafer. Section IV quantitatively assesses the waveguide continuous-wave (CW) power-damage thresholds, while presenting the microresonator thermal susceptibility and a quantitative contamination analysis of the fabricated structures, necessary for the understanding of residual background loss mechanisms and their origin.

2. Fabrication of ultralow-loss Si_3N_4-based photonics circuits

2.1. Film deposition

When compared to the most recent literature, the lowest attenuation coefficient reported for tightly confining 1.5-μm-wide Si_3N_4 waveguides is as low as 5.5–6.5 dB/m [18]. In contrast with the photonic Damascene processing, in our case the Si_3N_4 films have been deposited using the technique already published in [19,20]. This approach, that we later named *twist-and-grow* process, provides high thickness (> 1 μm) film deposition capabilities by coping with the high tensile strain otherwise causing the cracking of such films. This capability becomes particularly interesting when thicker films have to be deposited for many applications, ranging from III-V/SiN laser cointegration, integrated quantum photonics, and optical frequency combs. Such a characteristic provides outstanding flexibility to our platform when applied to different Si_3N_4 -based photonics circuits process design kits (PDK). Below, we explain how we optimized the processing of such films to make the most of this platform, and reach, in particular, very high quality factor microrings ×100 times higher with respect to our prior works [19,20].

2.2. Patterning and wafer bow management

The fabrication process starts with a 3-μm-thick thermal oxidation of a 200-mm diameter silicon substrate. Then a 800-nm-thick silicon nitride layer (Si_3N_4) is deposited by low-pressure chemical vapor deposition (LPCVD) following a tailored deposition method the authors published in [19,20], which minimizes the hydrogen content and prevents the deposited Si_3N_4 from cracking as shown in Figs. 1(a) and 1(b) mainly due to its inherent high-tensile strain. This twist-and-grow LPCVD technique presents the advantages of depositing relatively thick, pure and stoichiometric Si_3N_4 unlike standard PECVD techniques that suffer from intrinsic bulk absorption notably in the C band due to N-H bonds overtone absorption, regardless its advantage of a reduced film strain.

Concerning the Si_3N_4 patterning, a 248-nm deep-UV lithography is then performed using 820-nm-thick resist mask preceded by a 49-nm-thick bottom anti-reflection coating (BARC), [Fig. 1(c)]. This BARC layer uses destructive interferences in order to prevent additional roughness due to the back-reflected light during photo-lithography step. Prior to the Si_3N_4 etching, the photoresist patterns are cured with a HBr plasma in order to increase their resistance to the etching plasma, and thus to improve the etch selectivity [21]. The BARC layer is first opened with an $Ar/Cl_2/O_2$ plasma process, the Si_3N_4 is then etched with a $CF_4/CHF_3/Ar$ plasma in an inductively coupled plasma (ICP) reactor. The etch selectivity between the Si_3N_4 and the cured resist is 1.2:1. By adjusting the etching recipe parameters - notably reaction gases flux and chuck bias power - we were able to ensure slower etching rates (~ 4 nm/s) leading to a sufficient selectivity to the Si_3N_4 towards the resist mask, resulting in vertical waveguide sidewalls (< 1° sidewall slope) and accurate dimensional control. The resist mask and the fluorocarboned polymers present on the Si_3N_4 sidewalls after etching are then removed by an O_2 plasma process performed in a magnetically enhanced reactive ion etching (MERIE) reactor connected to the ICP reactor by vacuum transfer chamber. After plasma patterning, the Si_3N_4 surfaces are cleaned

Optics EXPRESS

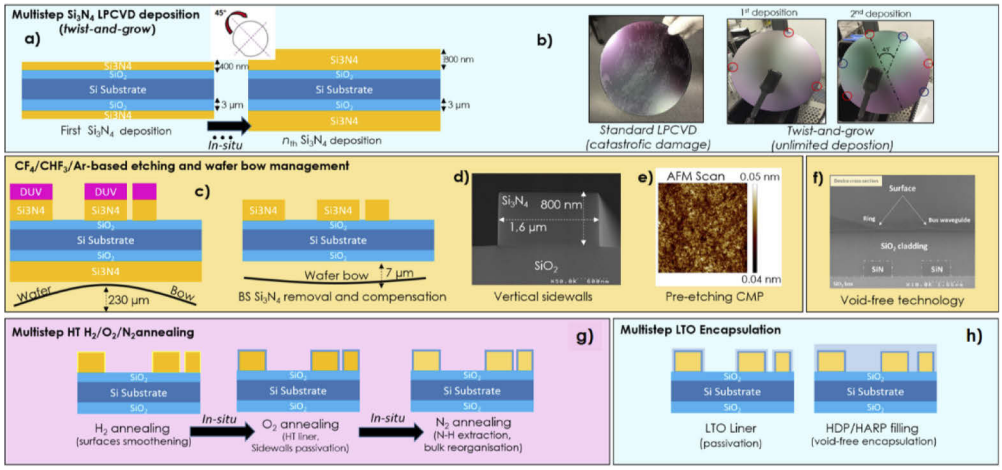

Fig. 1. Schematics of the *twist-and-grow* and multistep chemical-physical annealing process for ultralow-loss tightly confining Si_3N_4 waveguides. a) A 3-µm-thick wet oxidation of 200-mm Si wafer is followed by a *twist-and-grow* deposition of Si_3N_4 films until matching the desired film thickness (800 nm). b) Images of Si_3N_4 films with and without using this approach. c) Fluorocarbon-based dry etching and wafer bow compensation and d) reduction of top waveguide roughness to sub-Angstrom levels by CMP on the non-patterned films. e) Example of a 1.6-µm-wide, 800-nm-thick Si_3N_4 waveguide using CMP and fluorocarbon-based plasma etching process, with sidewalls slope angle < 2°. f) SEM cross-section of the encapsulated bus waveguide and microresonator. g) Multistep $H_2/O_2/N_2$ *in-situ* annealing of patterned core Si_3N_4 waveguides. h) Multistep encapsulation via a low-temperature silicon dioxide liner prior to high-density plasma silica layers encapsulation.

by a H_2SO_4-based wet solution. Figure 1(d) highlights the good quality of the plasma patterning process developed in this study, resulting in the waveguide well-shaped anisotropic profiles, free of residues.

It is worth mentioning that in our previous work [19], the $CF_4/CH_2F_2/O_2$ plasma process used to pattern the Si_3N_4 waveguide systematically results in the presence of polymer residues on the silicon nitride sidewalls and at the bottom of critical high-aspect ratio regions, such as the coupling gap between the bus waveguide and the microresonator. Polymer residues then inevitably bring in an increase in the line edge roughness [22,23] and organic contamination in critical regions of such architectures.

A proposed solution has been to increase the flow of oxygen to reduce the polymer residues thickness [22]. However, in this case, the oxygen would thin down the photoresist, leading to a selectivity decrease, resulting in an increased sidewall roughness. This would also impose limited sub-micrometric waveguide thickness, trapezoidal waveguide profiles, thus causing the unpredictability of the extrinsic loss rate $\kappa_{ex}/2\pi$ (*i.e.*, the power loss from the resonator to the bus waveguide). The $CF_4/CH_2F_2/O_2$ plasma showing some process limitations, a less polymerizing plasma chemistry using CHF_3 instead of CH_2F_2 is advantageously used in this work. Also, the CHF_3 has been added to CF_4 since it has a high C/F ratio so it could form polymers that compensate the highly isotropic etching of CF_4. Moreover, adding argon enhances the straight waveguides profiles by strong bombardment as well as the higher RF [24].

After patterning, the wafer has a quite high bow of 230µm that needs to be compensated to allow the wafer to continue the fabrication process. The bow is due to the presence of the tensile Si_3N_4 on the wafer backside. Often not carefully analyzed, the impact of wafer bow throughout the process flow is crucial, especially on large throughput platforms using mainly 200- and

Optics EXPRESS

300-mm wafers. The accumulation of compressive (typical for wet-oxidized SiO_2) and tensile strain of the Si_3N_4 film stacks, causes strong deformations of the silicon carrier substrates. Such wafer bow, which can grow up to 250–350 µm, may not only induce some damage of the film, but also eye-invisible sub-micrometric cracks along the waveguides after patterning. As shown in Fig. 1(c), this can be managed by a selective back removal of the Si_3N_4 film remaining on the wafer backside after patterning the front side. This ensures an almost ultra-flat wafer, with wafer bow values down to a few microns only (measured bow ~ 7 µm on a cross-wafer average), opening also interesting perspectives for Si_3N_4 on Si photonics cointegration by wafer bonding. Still, compared to the high-tensile stress observed in the case of strained PECVD films (1735 MPa for a 600 nm-thick SiN layer) [25], the wafer bow using our deposition technique remains manageable. Focusing on scattering-related losses, the attenuation coefficient (α, expressed in dB/m) of a waveguide depends on both sidewalls, top and bottom roughness of the waveguide [26]. In fact, before the waveguide patterning, we used an atomic force microscope (AFM) to measure the surface roughness of the as-deposited films. The AFM measurements revealed 0.4 nm of surface roughness of the Si_3N_4 films without any treatment. In order to reduce this surface roughness to a sub-Angstrom amplitude, a full-sheet 10-nm-deep CMP is carried out on the unpatterned wafers. As it could be seen from Fig. 1(d), the surface roughness is now reduced from 0.4 nm to ~ 0.1 nm (or 1 Å, which is approximately the resolution limit of the AFM measurement) by the sole beneficial action of shallow CMP. The as-etched Si_3N_4 waveguides present a mean square left/right sidewalls roughness in the range of 1.2–1.3 nm, confirmed by tilted-AFM [27] and critical dimension scanning electron microscopy (CD-SEM) [28] morphological observations.

2.3. Multistep chemical-physical annealing of Si_3N_4 waveguides

The stoichiometric silicon nitride deposited by low-pressure chemical vapor deposition (LPCVD) is not totally hydrogen-free [20,29] even when using ultra-low deposition rates that aim at minimizing such hydrogen content. Although optical frequency combs could be obtained without annealing the waveguides [29], reemphasizing the high quality of such as-deposited material, the quality factors of the resulting microrings were limited to a few hundreds of thousands in the C-band. In order to reduce the attenuation coefficient to the lowest possible value, we developed in this work a multiple-step chemical-physical *in-situ* high-temperature annealing sequence using H_2, O_2, and N_2 following the waveguide patterning. The N_2 and O_2 annealings were performed in the same tube at ambient pressure, whereas the hydrogen annealing was performed in a vertical epitaxial chamber at 10 Torr. We detail the different steps of this optimized annealing sequence in the three paragraphs below.

Recent studies have shown the pure hydrogen streams capability to smoothen out the sidewall roughness of single-mode silicon waveguides for TE-operation to record-low values, when operating such H_2 annealing at particular pressure, temperature, and time exposure conditions [30].

By following the same rationale, we first applied a flash (*i.e.*, a few minutes long) 1100°C hydrogen-based annealing in order to induce morphological modification of the waveguide. The beneficial effect of such treatment is analyzed via morphological and optical characterization tests in the next section.

As a second operation, the waveguides are exposed to a full O_2-based 1200 °C annealing for a few minutes. This step is aimed at reducing surface states through the effective passivation and mechanically-robust encapsulation of the waveguide core via a dense, high-temperature, native oxidation of the silicon nitride surface, precluding the formation of intra-gap scattering absorption centers.

Finally, the silicon nitride film should be densified through driving out the hydrogen excess and breaking N-H bonds in order to get closer to a stoichiometric Si_3N_4 film, reducing, in turn, the material absorption loss in the C-band. However, we did not observe any remarkable thickness

Optics EXPRESS

variation before and after the annealing sequence. This finding is based on SEM cross-sectional thickness of the waveguide before and after the annealing sequence. Such a fact is due to the small hydrogen dimension as element, to a point that, although when hydrogen is driven out of the film by the multi-step annealing treatments, no layer thickness variation could be observed. A pure nitrogen annealing is applied on the un-cladded waveguides (1200 °C for 3 hours) in order to drive out the residual hydrogen, breaking N-H bonds and reducing their residual population. This provides sufficient activation energy to reorganize the bulk structure of the waveguide in order to minimize the presence of bulk defect states, otherwise causing detrimental bulk absorption [Fig. 1(g)].

2.4. Multistep NO/LTO encapsulation

Generally, proper mineral void-free encapsulation of the device provides the necessary optical properties for achieving ultralow-loss light propagation. Although it might seem trivial, for the annealing procedure, we perform a multiple step encapsulation at low-temperature oxide deposition (LTO, 400 °C) consisting first of a tetraethyl orthosilicate (TEOS)-based low-rate liner deposited on top of the native oxidized (NO) surface. Following that, as shown in Fig. 1(h), several liners of high-density silica were deposited in order to achieve void-free encapsulation thanks to the alternated phases of etching and proper filling of high-density plasma enhanced chemical vapor deposition (HDP-ECVD). This procedure allows us to achieve, simultaneously, a) a proper native oxide interface of the waveguide, b) a protection against HDP-plasma ions bombardment on the top of the waveguide as well as along its sidewalls, and, lastly, c) a void-free encapsulation of critical high-aspect ratio regions, especially in the coupling region between the bus and the resonator (Fig. 1(f)). Furthermore, a void-free encapsulation is critical in order to guarantee a reduced scattering at the coupling region, minimizing systematic excess losses due to the inter-mode interactions, and increasing the threshold power of failure events. This is of the utmost importance, especially in the perspective of the co-integration of III-V-based reflective semiconductor amplifiers (RSOAs) or even free-running multimode laser sources butt-coupled to ultra-high Q Kerr microresonators for compact, chip-based and power-efficient optical frequency comb sources [31–36].

3. Optical characterization and statistical analysis

In order to evaluate the impact of the different processing steps presented in the previous section on the Si_3N_4 microresonator performance and their statistical cross-wafer dispersion, the ring resonators are optically characterized via TE-polarization surface grating couplers (SGCs) on a 300-mm fiber probing station, providing an input/output (I/O) insertion loss of the SCGs in the order of approximately 6 dB each. In this study, TE-polarization has been chosen mainly because of the grating couplers operating in TE-mode and especially because a semi-automated probing station using grating couplers fiber arrays was used. Such a method ensures an extensive statistical analysis of devices features across several dies of the entire 200-mm wafer. This was less time-consuming then operating in edge-coupling configuration, where a die-by-die approach would have been needed. A tunable laser source delivering a stable 1 mW input power is used for direct resonance scanning across the S-, C- and L-bands, with a wavelength tuning step of 0.1 pm (12.5 MHz) which is the minimum wavelength sampling step of our laser source. A −20 dB optical attenuator is used before coupling to the chip in order to precisely assess the resonance spectral characteristics (*i.e.*, the resonance linewidth) at low dropped power levels to the microring, in order to suppress the resonance skewing coming from the thermal susceptibility χ_{th} of the microresonator [16].

Optics EXPRESS

The intrinsic quality factors are extracted by fitting the measured resonance transmission with the following doublet model:

$$T = \left[1 - \frac{\kappa_{ex}/2\pi}{2(i(f-f_1) + \kappa_{01}/2\pi + \kappa_{ex}/2\pi)} - \frac{\kappa_{ex}/2\pi}{2(i(f-f_2) + \kappa_{02}/2\pi + \kappa_{ex}/2\pi)}\right]^2,$$

where $\kappa_{01}/2\pi$ and $\kappa_{02}/2\pi$ are the intrinsic linewidths of the clockwise (CW) and counterclockwise (CCW) modes in the resonator, while f_1 and f_2 are the resonant frequencies of the two modes in the resonator.

The measurement setup scheme as well as a top-view optical micro cope image of the ring resonators are shown in Figs. 2(a) and 2(b).

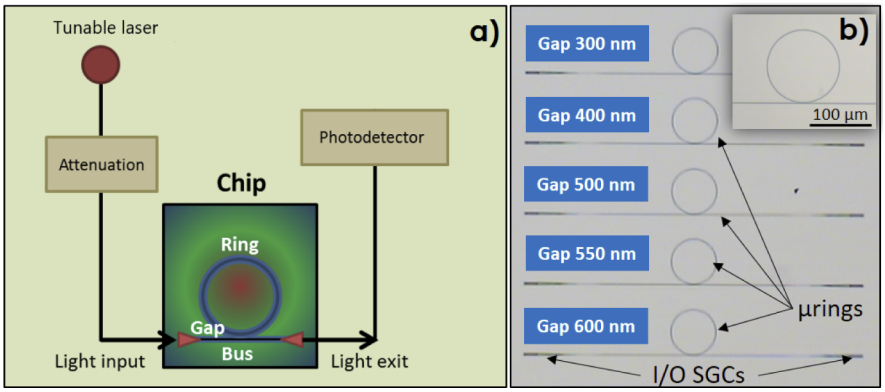

Fig. 2. Schematic representation of a) the optical measurement setup used for the characterization of microresonators and test structures. Direct laser scanning spectroscopy is carried out using a high-sensitivity photodetector. b) Microscope image of the 200-GHz-FSR ring resonators with different bus/ring gap configurations. Input/output (I/O) signal is collected via surface grating couplers (SGCs) operating in TE-polarization.

3.1. Attenuation coefficient derivation via undercoupled resonators spectrum analysis

TE-polarized light is injected in the bus waveguide via the input SCGs, and then coupled into a series of nominally identical microrings using different gaps separating the ring resonator from the waveguide to yield different microresonator loading regimes. The waveguide cross-sectional dimension ($w \times h$) is 1.63 µm × 0.8 µm, while five different coupling gaps are tested from 300 nm up to 600 nm, in order to access to a statistical distribution of the device performance across overcoupled, critically coupled, and undercoupled regimes. The undercoupled configuration is the most suitable to assess the intrinsic quality factors Q_0 and linewidths $\kappa_0/2\pi$ as well as attenuation losses α_i (dB/m) of the microresonator waveguides [18], while the critically coupled regime maximizes the loading to the microresonators and the extinction ratios between the on and out of resonance transmission. In Fig. 2(b), we show a microscope image of a typical chipset containing the five configurations tested of 200-GHz free spectral range (FSR) 110-µm-radius microresonators.

The results in Fig. 3(a) show the unclad waveguide sidewalls roughness measured by CD-SEM data analysis at different stages of the waveguide processing, and for different post-patterning annealing treatments. First, the sidewall roughness decreases from around 4 nm after lithography down to barely 1.25 nm just after the Si_3N_4 waveguides etching. As another evidence of the high quality of the patterning process developed in this work, the resulting waveguides exhibit well-shaped anisotropic profiles as already shown in Fig. 1(d). Moreover, three different

Optics EXPRESS

high-temperature post-patterning thermal treatments under different chemical environments are then compared in Fig. 3(a). More specifically, we labeled these chemical-physical thermal treatments as follows: a) treatment T_1 (using just 100% N_2 at 1200°C for 3 hours), b) treatment T_2 (using 99% N_2+1% O_2 at 1200°C for 3 hours) and, lastly, c) treatment T_3 (1100 °C flash annealing under H_2 followed by 100% O_2 annealing for 20 minutes and 100% N_2 for 3 hours, with the latest two both carried out at 1200 °C). As noticed from Fig. 3(a), these three post-treatments do not have any remarkable effect on the sidewall roughness compared to the as-etched devices, except for a slight enhancement when using flash-annealing under pure H_2 atmosphere (wafer T_3) where the RMS value reaches ~ 1 nm. This treatment will actually reveal itself as decisive in achieving ultralow attenuation waveguides.

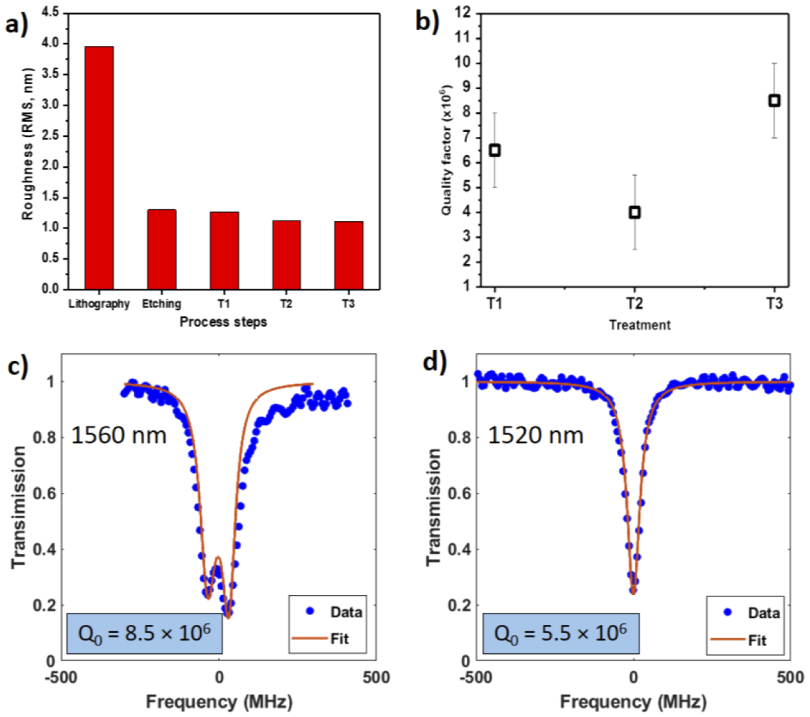

Fig. 3. (a) Waveguide sidewalls roughness evolution during the fabrication process (lithography, dry etching) including comparison between different post-etching annealing strategies (T_1, T_2, and T_3). (b) Quality factors and their corresponding standard deviations as a function of the annealing treatment used. The data show average and statistical dispersion of Q_0 values in the wavelength interval 1550–1570 nm, centered at 1560 nm and sampled across 20 different dies. c) Resonance doublet at $\lambda = 1560$ nm with an extracted fitted intrinsic linewidth $\kappa_0/2\pi$ of 23 MHz corresponding to an intrinsic $Q_0 \sim 8.5\times10^6$, and fitted splitting rate $\Omega/2\pi = 62$ MHz (wafer T_3). d) Resonance at $\lambda = 1520$ nm with a fitted intrinsic linewidth $\kappa_0/2\pi$ of 36 MHz corresponding to an intrinsic $Q_0 \sim 5.3\times10^6$.

In order to evaluate the attenuation coefficient of the resonator waveguides on wafer T_3 (which underwent the H_2 annealing treatment) via the intrinsic quality factors, we started the analysis of resonators operating in the undercoupled regime, in order to minimize the contribution from the excess losses caused by coupling non-ideality, and thus have the internal loss rate $\kappa_0/2\pi$ dominating the total loss rate. In detail, the analysis is performed by measuring the resonance linewidths from the transmission spectrum. This provides the resonator total loss rate $\kappa/2\pi = (\kappa_0 + \kappa_{ex})/2\pi$, which is the sum of the coupling loss rate $\kappa_{ex}/2\pi$ from the bus to the microring and

Optics EXPRESS

the intrinsic microresonator loss rate $\kappa_0/2\pi$. Undercoupled resonators were found only for the maximum available gap on the maskset (*i.e.*, a gap width of 600 nm). As shown in Figs. 3(c) and 3(d), resonance doublets, coming from the coherent backscattering in the microresonator could be easily observed all across the wafer for such coupling rate. The intrinsic quality factor is deduced using a spectrally-resolved resonance doublet (with a splitting rate higher than the setup resolution) to be sure that we are not extracting the quality factor from a doublet with a splitting rate lower than the resolution of our setup, and then considering the resonance as a simple Lorenzian. As shown in Fig. 3(c), by using resonant doublet line shape fitting model, an intrinsic loss rate $\kappa_0/2\pi$ of 23 MHz could be extracted from measurements, corresponding to an intrinsic quality factor $Q_0 \sim 8.5\times10^6$ at 1560 nm wavelength (C-band), and a fitted splitting rate $\Omega/2\pi = 60$ MHz.

By repeating the same measurement at 1520 nm (S band) shown in Fig. 3(d), we extracted an intrinsic linewidth of 36 MHz corresponding to a Q_0 of $\sim 5.3 \times 10^6$. This indicates that the residual N-H overtone absorption from the Si_3N_4 material was almost totally eliminated from the waveguides through the *in-situ* annealing steps. However, when comparing Figs. 3(c) and 3(d), the increase in losses at this blue-shifted wavelength comes though from the overtone absorption of residual N-H bonds population still present in the film, and responsible for a difference of about 22 MHz in the intrinsic linewidths between 1520 nm and 1560 nm. In fact, at 1520 nm, the quality factors remained high as an indication that the high-temperature treatment along with the $H_2/O_2/N_2$ ambient was efficient to eliminate a major part of N-H bonds. Still, since the quality factors decrease by shifting to blue, N-H bonds residual population exist, though in a reduced amount. Figure 3(b) shows the average intrinsic quality factors with their corresponding standard deviations extracted from these measurements, comparing the use of the three different annealing treatments T_1, T_2 and T_3. In particular, the values report average and statistical dispersion of Q_0 values in the wavelength interval of 20 nm centered at 1560 nm, and sampled across 20 different dies on each wafer (T_1, T_2 and T_3). Notably, from these results we can infer that the best attenuation coefficient α has been obtained on wafer T_3, which underwent the flash H_2-annealing treatment. As already alluded to, the T_3 treatment leads to an increase of the measured intrinsic Q_0 factor with respect to the other two annealing processes. This can be explained by the fact that this treatment allows a further smoothening (although minor) of the waveguides as reported in Fig. 3(a), and, therefore, a strong reduction in scattering-related losses.

The attenuation coefficient of the waveguides can be inferred from analyzing the spectral properties of the microresonator resonances. The intrinsic Q_0 is related to the attenuation coefficient as $\alpha = \kappa_0 n_{\text{eff}}/c$ where κ_0 is the intrinsic losses rate and n_{eff} is the group index of the TE-polarization optical fundamental mode (1.79 in our case). Hence, this corresponds in our case to a waveguide attenuation coefficient at least as low as $\alpha \sim 3.5$ dB/m at 1560 nm wavelength with an uncertainty of 0.5 dB/m, which is the lowest propagation loss for high-confinement silicon nitride waveguides with similar cross-sectional dimensions reported so far at such wavelength (1560 nm) [18]. Note that such estimated propagation losses constitute a conservative estimate of the real attenuation coefficient, as we still operate at the very edge of the undercoupled regime using the maximum gap dimension available on the maskset. A second source of propagation losses overestimation comes from the fact that we are extracting loss from a microring instead of straight waveguides cut-back measurements. In a ring the optical mode interacts more with the sidewall roughness due to the bending, especially when operating in TE polarization.

In summary, the ultralow optical losses obtained for the $H_2/O_2/N_2$ multistep annealing and the sequential encapsulation treatment result from the combination of several intrinsic material and device patterning improvements. Namely, this comes from, firstly, a) the structural bulk reorganization and b) the dehydrogenation via N_2 annealing of the Si_3N_4 film, then c) an effective surface-state passivation and d) waveguide core protection against ion bombardment and mechanical shocks obtained through a controlled O_2 annealing, its native oxide (NO) and

Optics EXPRESS

LTO liners, and, finally, e) the decrease in scattering loss by sidewall smoothening via flash H_2 annealing.

3.2. Statistical analysis of critically coupled resonators

An extensive optical characterization of the devices was mandatory to study the impact of the different post-annealing treatments on the overall device performance. This includes the extinction ratio of in and out of resonance microring transmission, the intrinsic linewidth $\kappa_0/2\pi$ as well as the deviation in the as-fabricated resonant absolute wavelengths at 1561 nm of nominally identical microrings. As shown in Fig. 4(a), a statistical study is performed over the aforementioned five bus-to-ring gap configuration in order to discriminate against overcoupled (zone I), near critically coupled (zone II), and undercoupled devices (zone III). Such distribution of the devices over the aforementioned three zones is based on the extinction ratios of the microresonators. The undercoupled devices in zone III have a bus-to-microresonator coupling gap of 600 nm, which is the largest available on our maskset. On the other hand, devices using a coupling gap of 550 nm, statistically exhibit the highest extinction ratios, and thus operate near to critical coupling conditions at 1561 nm wavelength. We note that the analysis is carried out on the type-3 (T_3) wafer, which underwent flash H_2-annealing, and exhibits the lowest attenuation coefficient and waveguide sidewalls roughness values.

In order to estimate the high reproducibility of the optical losses and the quality factor following our fully subtractive fabrication process, a statistical study over 20 chips (part of the same 200-mm wafer) is made for the 550-nm-wide coupling gap, in order to operate near critical coupling conditions. These values have been averaged over multiple resonances measured in a wavelength interval of 20 nm centered at 1560 nm, and sampled across 20 different dies.

The value of the intrinsic linewidth $\kappa_0/2\pi$ shown in Fig. 4(c) in the nearby of 1560 nm reads out at an average value of 41.2 MHz, with a standard deviation of just 6.8 MHz. Also in this case, these values have been averaged over multiple resonances across a wavelength interval of 20 nm centered at 1560 nm wavelength. Moreover, as reported in Fig. 4(b), the intrinsic linewidths evolution of the 200-GHz FSR resonator as a function of the wavelength shows good uniformity across the S, C, and L bands (1500 nm −1600 nm). In Fig. 4(d), we plot also the single resonance variation across the same wavelength range from the average intrinsic linewidth.

Lastly, concerning the extinction ratios of the microresonators, when the gap between the ring and the bus waveguide is of 550 nm, more than 10 dB are obtained on 95% of tested devices, as shown in Fig. 4(e). Moreover, the mean calculated value for the extinction ratio is of 13.1 dB, with a standard deviation of just 2.1 dB sampled across the 200-mm wafer. Such results mirrors the high uniformity of the Si_3N_4 film thickness deposition, while supporting the high-reproducibility of the whole technology across a wafer.

Optics EXPRESS

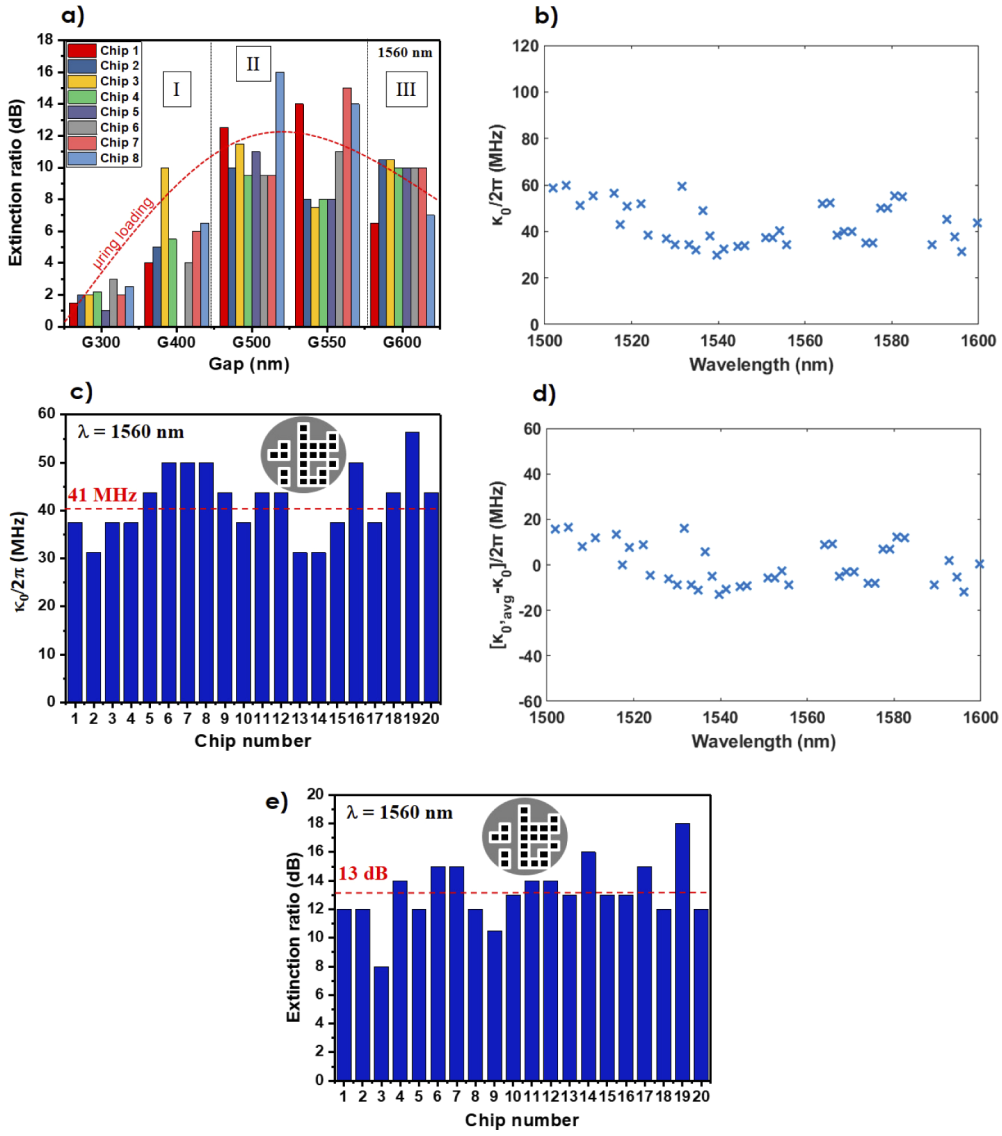

Fig. 4. (a) Extinction ratios cross-die vs. gap distribution of overcoupled (zone I), near to critically-coupled (zone II), and undercoupled (zone III) 200-GHz resonators devices. (b, d) Intrinsic linewidths (MHz) and their absolute variation against the average linewidth across the 1500–1600 nm wavelengths (S, C, and L bands), (c) intrinsic linewidths (MHz) and (e) extinction ratios of critically coupled devices (coupling gap = 550 nm) measured in a wavelength interval of 20 nm centered at 1560 nm, and sampled across 20 different dies (with respective average values indicated by a red dashed line). The 20 dies relative positions on the 200-mm T_3 wafer are indicated in the inset of (c, e).

Optics EXPRESS

4. Bulk absorption limitations, thermal susceptibility, and device reliability

As a final step to assess the origin of the microresonator residual losses beyond the sidewall roughness induced scattering, we studied and measured by total reflection X-ray fluorescence (TXRF) measurements the nature and relative concentration of metallic contamination contained in the Si_3N_4 film. In fact, the presence of such metallic elements may act as mid-gap scattering centers that are responsible for photon absorption both in the bulk and on the surface of the waveguide. Notably, a statistical dispersion over 125 wafers of metallic impurities concentration in the film was performed, with red dots indicating "outlier" measurement points. The red line (labeled as UCL) show the "upper contamination limit" allowed in a production-compatible CMOS pilot line, with 5×10^{10} atoms/cm^2 and 5×10^{11} atoms/cm^2 as hard limits imposed on the specific metal element. The results of Fig. 5(a) show that very low levels of contamination are present, notably Ca and K (10^{11} atoms/cm^2), while contamination coming from Fe, Co, Cr, Cu shows levels between 10^{10}–10^{11} atoms/cm^2. The presence of Ca and K is notably related to the residual contamination coming from the de-ionized water used for wafer cleaning, while Cu, Al, Ni, Ti come instead from CMOS-based contact metal technology. The origin of Fe, Al, Zn contamination may be related to both InP and GaAs epitaxial and substrate doping as well as III-V ternary and quaternary alloys compositions. The contamination levels detected in the film

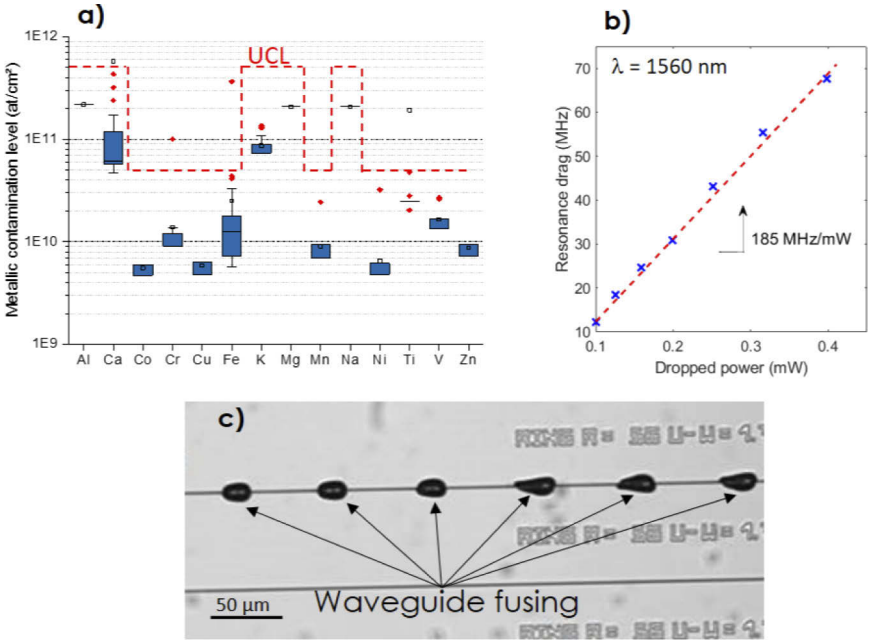

Fig. 5. (a) TXRF analysis of metallic contamination of as-deposited Si_3N_4 films described and processed in this work. Statistical dispersion over 125 wafers of metallic impurities in the film (blue boxes), with red dots indicating "outlier" measurement points. The red line (labeled as UCL) show the "upper contamination limit" allowed in a production-level CMOS pilot line, with 5×10^{10} atoms/cm^2 and 5×10^{11} atoms/cm^2 as hard limits imposed on the specific metal element. (b) Extracted resonance drags (MHz) for different dropped powers (mW) revealing the resonator thermal susceptibility χ_{th} = 185 MHz/mW at 1560 nm wavelength. (c) Image of a failure event when a CW input optical power of + 38 dBm is coupled to a Si_3N_4 waveguide. The failure event has been observed only once during measurements at such power levels. No failure event was observed on any microresonator during device testing at such high power levels.

Optics EXPRESS

used in this work are 6 to 7 orders of magnitude lower than the values reported for the Si_3N_4 –based photonic Damascene process [16]. Yet, we consider our contamination levels as standard for a production-compatible CMOS line.

This clearly opens up interesting prospects for identifying and reaching the ultimate limitations of Si_3N_4 bulk absorption and the consequent further reduction of the waveguide attenuation coefficient. Moreover, a low contamination level helps in reducing the thermal susceptibility of the devices, which is, for instance, of great importance for the stability of quantum optics devices under operation. Obviously, the thermal susceptibility χ_{th} of the ultralow-loss Si_3N_4 integrated resonators is related to the bulk density of metal contaminants that act as scattering centers for non-radiative recombination events, mainly producing phonon emission. The thermal susceptibility is, in turn, related to the absorption loss rate and the overall contribution of non-scattering related losses of the waveguide [16]. As reported in Fig. 5(b), we extracted χ_{th} from the linear correlation of the resonance drag (in MHz) vs the power dropped to the ring (in mW). This reveals a thermal susceptibility χ_{th} of the microresonator of 185 MHz/mW for a critically coupled resonator at 1560 nm wavelength. This value is about $\sim$ 30% smaller than previously reported [16, Fig. 3(b)] when comparing the same methodology and data for the χ_{th} extraction.

Power-damage thresholds are also very important to assess the reliability and aging of the device. Extensive optical tests under continuous-wave injection at power levels up to + 20 dBm were carried out on the same chips for over 3 months, with no visible change over the spectral (and material) properties of the microresonators. Devices underwent also stress test at very high continuous-wave power levels, with coupled powers to the bus waveguide of approximately + 40 dBm. No failure event of a microresonator has been observed over the whole test duration for such power levels. However, a single failure event happened for a bus waveguide, the results of which is shown Fig. 5(c). More precisely, the fuse started from the left-hand side of the chip, where optical coupling between input lensed fiber and the Si_3N_4 waveguide was performed.

5. Conclusions and perspectives

In this work we presented both the fabrication and testing of high-confinement ultralow-loss Si_3N_4 waveguides and high-Q microresonators showing attenuation coefficients as low as ~3–3.5 dB per meter and intrinsic quality factors approaching $\sim 10^7$ across the C band, respectively. These devices exhibit very low deviations in their performance with a high uniformity on a 200-mm full-wafer scale, low thermal susceptibility, and high-power CW damage thresholds. This was made possible thanks to the development of an optimized fully subtractive process introducing a novel chemical-physical multistep annealing and a carefully tailored encapsulation process. This technology produces high quality Si_3N_4-based optical circuits that are well-suited for energy-efficient nonlinear photonics and integrated quantum optics.

Funding

H2020 European Research Council; Agence Nationale de la Recherche; Commissariat à l'Énergie Atomique et aux Énergies Alternatives.

Acknowledgments

The authors also gratefully acknowledge Prof. Marco Liscidini from University of Pavia for providing insightful remarks, contributing to a substantial improvement of the paper.

References

1. A. Politi, M. J. Cryan, J. G. Rarity, S. Yu, and J. L. O'Brien, "Silica-on-silicon waveguide quantum circuits," Science **320**(5876), 646–649 (2008).

Optics EXPRESS

2. S. Ramelow, A. Farsi, Z. Vernon, S. Clemmen, X. Ji, J. E. Sipe, M. Liscidini, M. Lipson, and A. L. Gaeta, "Strong nonlinear coupling in a Si_3N_4 ring resonator," Phys. Rev. Lett. **122**(15), 153906 (2019).
3. F. Dell'Olio, T. Tatoli, C. Ciminelli, and M. N. Armenise, "Recent advances in miniaturized optical gyroscopes," J. Eur. Opt. Soc. **9**, 14013 (2014).
4. M. Belt, J. Bovington, R. Moreira, J. F. Bauters, M. J. Heck, J. S. Barton, J. E. Bowers, and D. J. Blumenthal, "Sidewall gratings in ultra-low-loss Si_3N_4 planar waveguides," Opt. Express **21**(1), 1181 (2013).
5. T. Herr, K. Hartinger, J. Riemensberger, C. Y. Wang, E. Gavartin, R. Holzwarth, M. L. Gorodetsky, and T. J. Kippenberg, "Universal formation dynamics and noise of Kerr-frequency combs in microresonators," Nat. Photonics **6**(7), 480–487 (2012).
6. P. Marin-Palomo, J. N. Kemal, M. Karpov, A. Kordts, J. Pfeifle, M. H. Pfeiffer, P. Trocha, S. Wolf, V. Brasch, M. H. Anderson, and R. Rosenberger, "Microresonator-based solitons for massively parallel coherent optical communications," Nature **546**(7657), 274–279 (2017).
7. W. Liang, D. Eliyahu, V. S. Ilchenko, A. A. Savchenkov, A. B. Matsko, D. Seidel, and L. Maleki, "High spectral purity Kerr frequency comb radio frequency photonic oscillator," Nat. Commun. **6**(1), 7957 (2015).
8. D. T. Spencer, T. Drake, T. C. Briles, J. Stone, L. C. Sinclair, C. Fredrick, Q. Li, D. Westly, B. R. Ilic, A. luestone, and N. Volet, "An optical-frequency synthesizer using integrated photonics," Nature **557**(7703), 81–85 (2018).
9. H. Lee, T. Chen, J. Li, K. Y. Yang, S. Jeon, O. Painter, and K. J. Vahala, "Chemically etched ultrahigh-Q wedge-resonator on a silicon chip," Nat. Photonics **6**(6), 369–373 (2012).
10. N. G. Pavlov, S. Koptyaev, G. V. Lihachev, A. S. Voloshin, A. S. Gorodnitskiy, M. V. Ryabko, S. V. Polonsky, and M. L. Gorodetsky, "Narrow-linewidth lasing and soliton Kerr microcombs with ordinary laser diodes," Nat. Photonics **12**(11), 694–698 (2018).
11. M. J. Weber, D. Milam, and W. L. Smith, "Nonlinear refractive index of glasses and crystals," Opt. Eng. **17**(5), 463 (1978).
12. X. Ji, A. B. Felippe, S. P. Roberts, A. Dutt, J. Cardenas, Y. Okawachi, A. Bryant, A. L. Gaeta, and M. Lipson, "Ultra-low-loss on-chip resonators with sub-milliwatt parametric oscillation threshold," Optica **4**(6), 619 (2017).
13. Y. Xuan, Y. Liu, L. T. Varghese, A. J. Metcalf, X. Xue, P. H. Wang, K. Han, J. A. Jaramillo-Villegas, A. Al Noman, C. Wang, and S. Kim, "High-Q silicon nitride microresonators exhibiting low-power frequency comb initiation," Optica **3**(11), 1171 (2016).
14. D. T. Spencer, J. F. Bauters, M. J. R. Heck, and J. E. Bowers, "Integrated waveguide coupled Si_3N_4 resonators in the ultrahigh-Q regime," Optica **1**(3), 153 (2014).
15. T. Herr, V. Brasch, J. Jost, I. Mirgorodskiy, G. Lihachev, M. Gorodetsky, and T. J. Kippenberg, "Mode spectrum and temporal soliton formation in optical microresonators," Phys. Rev. Lett. **113**(12), 123901 (2014).
16. M. H. P. Pfeiffer, J. Liu, A. S. Raja, T. Morais, B. Ghadiani, and T. J. Kippenberg, "Ultra-smooth silicon nitride waveguides based on the Damascene reflow process: fabrication and loss origins," Optica **5**(7), 884 (2018).
17. M. H. P. Pfeiffer, J. Liu, M. Geiselmann, and T. J. Kippenberg, "Coupling ideality of integrated planar high-Q microresonators," Phys. Rev. Appl. **7**(2), 024026 (2017).
18. M. H. P. Pfeiffer, C. Herkommer, J. Liu, T. Morais, M. Zervas, M. Geiselmann, and T. J. Kippenberg, "Photonic Damascene process for low-loss, high-confinement silicon nitride waveguides," IEEE J. Sel. Top. Quantum Electron. **24**(6), C4 (2018).
19. H. El Dirani, M. Casale, S. Kerdiles, C. Socquet-Clerc, X. Letartre, C. Monat, and C. Sciancalepore, "Crack-free silicon-nitride-on-insulator nonlinear circuits for continuum generation in the C-band," IEEE Photonics Technol. Lett. **30**(4), 355–358 (2018).
20. H. El Dirani, A. Kamel, M. Casale, S. Kerdiles, C. Monat, X. Letartre, M. Pu, L. K. Oxenløwe, K. Yvind, and C. Sciancalepore, "Annealing-free Si_3N_4 frequency combs for monolithic integration with Si photonics," Appl. Phys. Lett. **113**(8), 081102 (2018).
21. L. Azarnouche, E. Pargon, K. Menguelti, M. Fouchier, O. Joubert, P. Gouraud, and C. Verove, "Benefits of plasma treatments on critical dimension control and line width roughness transfer during gate patterning," J. Vac. Sci. Technol., B **31**(1), 012205 (2013).
22. D. Beery, K. Reinhardt, P. B. Smith, J. Kelley, and A. Sivasothy, "Post etch residue removal: novel dry clean technology using densified fluid cleaning (DFC)," in *IEEE International Interconnect Technology Conference (Cat. No. 99EX247)* (1999), pp. 140–142.
23. M. Schaepkens, T. E. F. M. Standaert, N. R. Rueger, P. G. M. Sebel, G. S. Oehrlein, and J. M. Cook, "Study of the SiO_2-to-Si_3N_4 etch selectivity mechanism in inductively coupled fluorocarbon plasmas and a comparison with the SiO_2-to-Si mechanism," J. Vac. Sci. Technol., A **17**(1), 26–37 (1999).
24. J. H. Ye and M. S. Zhou, "Carbon-rich plasma induced damage in silicon nitride etch," J. Electrochem. Soc. **147**(3), 1168–1174 (2000).
25. G. Kissinger, D. Kot, I. Costina, and M. Lisker, "On the impact of strained PECVD nitride layers on oxide precipitate nucleation in silicon," ECS J. Solid State Sci. Technol. **8**(9), N125–N133 (2019).
26. F. P. Payne and J. P. R. Lacey, "A theoretical analysis of scattering loss from planar optical waveguides," Opt. Quantum Electron. **26**(10), 977–986 (1994).
27. M. Fouchier, E. Pargon, and B. Bardet, "An atomic force microscopy-based method for line edge roughness measurement," J. Appl. Phys. **113**(10), 104903 (2013).

Optics EXPRESS

28. L. Azarnouche, "Challenges in reducing the roughness of 193 nm photoresist patterns," PhD thesis from University of Grenoble (2012).
29. J. Z. Xie, "Stability of hydrogen in silicon nitride films deposited by low-pressure and plasma enhanced chemical vapor deposition techniques," J. Vac. Sci. Technol. B Microelectron. Nanom. Struct. **7**(2), 150 (1989).
30. C. Bellegarde, E. Pargon, C. Sciancalepore, C. Petit-Etienne, V. Hughes, D. Robin-Brosse, J.-M. Hartmann, and P. Lyan, "Improvement of sidewall roughness of sub-micron SOI waveguides by hydrogen plasma and annealing," IEEE Photonics Technol. Lett. **30**(7), 591–594 (2018).
31. B. Stern, X. Ji, Y. Okawachi, A. L. Gaeta, and M. Lipson, "Fully integrated ultra-low power Kerr comb generation," Nature **562**(7727), 401–405 (2018).
32. A. Matsko, A. Savchenkov, D. Strekalov, V. Ilchenko, and L. Maleki, "Optical hyperparametric oscillations in a whispering-gallery-mode resonator: threshold and phase diffusion," Phys. Rev. A **71**(3), 033804 (2005).
33. S. A. Raja, A. Voloshin, H. Guo, S. Agafonova, J. Liu, A. S. Gorodnitskiy, M. Karpov, N. G. Pavlov, E. Lucas, R. R. Galiev, A. E. Shitikov, J. D. Jost, M. L. Gorodetsky, and T. J. Kippenberg, "Electrically pumped photonic integrated soliton microcomb," Nat. Commun. **10**(1), 680 (2019).
34. A. L. Gaeta, M. Lipson, and T. J. Kippenberg, "Photonic-chip-based frequency combs," Nat. Photonics **13**(3), 158–169 (2019).
35. S. Boust, H. El Dirani, F. Duport, L. Youssef, S. Kerdiles, Y. Robert, C. Petit-Etienne, M. Faugeron, E. Vinet, M. Viallet, E. Pargon, C. Sciancalepore, and F. Van Dijk, "Compact optical frequency comb source based on a DFB butt-coupled to a silicon nitride microring," *IEEE Microwave Photonics Conference*, (2019).
36. J. Liu, A. S. Raja, M. Karpov, B. Ghadiani, M. H. P. Pfeiffer, B. Du, N. J. Engelsen, H. Guo, Mi. Zervas, and T. J. Kippenberg, "Ultralow-power chip-based soliton microcombs for photonic integration," Optica **5**(10), 1347–1353 (2018).